

# Power spectrum of passive scalars in two dimensional chaotic flows

Guo-Cheng Yuan

*Department of Mathematics and Institute for Physical Science and Technology, University of Maryland, College Park, Maryland 20742*

Keeyeol Nam, Thomas M. Antonsen, Jr.,<sup>a)</sup> and Edward Ott<sup>a)</sup>

*Department of Physics and Institute for Plasma Research, University of Maryland, College Park, Maryland 20742*

Parvez N. Guzdar

*Institute for Plasma Research, University of Maryland, College Park, Maryland 20742*

(Received 2 April 1999; accepted for publication 8 June 1999)

In this paper the power spectrum of passive scalars transported in two dimensional chaotic fluid flows is studied theoretically. Using a wave-packet method introduced by Antonsen *et al.*, several model flows are investigated, and the fact that the power spectrum has the  $k^{-1}$ -scaling predicted by Batchelor is confirmed. It is also observed that increased intermittency of the stretching tends to make the roll-off of the power spectrum at the high  $k$  end of the  $k^{-1}$  scaling range more gradual. These results are discussed in light of recent experiments where a  $k^{-1}$  scaling range was not observed. © 2000 American Institute of Physics. [S1054-1500(00)00701-1]

**Transport of passive scalars (such as impurities) is important in a number of areas including geoscience, weather prediction, and control of industrial pollutants. When an external long wavelength source continually injects passive scalars into a chaotic flow, small spatial structures will develop due to the straining motion in the flow. Thus the time asymptotic state contains a broad range of length scales. In this paper we numerically investigate the wave number ( $k$ ) power spectrum of a passive scalar field. Our results are in good agreement with Batchelor's theoretical prediction of the scaling of the power spectrum as  $k^{-1}$  until a high  $k$  diffusive cutoff region. We find that the  $k$  dependence of the spectrum in the cutoff region depends on the properties of the flow (in particular intermittency of the flow has an important effect). A theory based on chaotic straining of wave packets is employed to explain these observations.**

## I. INTRODUCTION

We consider passive advection of a weakly diffusive scalar quantity (e.g., temperature or the concentration of an impurity) in an irregular, time varying fluid flow. Due to the straining motion of the flow, small fluid regions are stretched and eventually folded as time evolves. As a result, finer and finer spatial structure of the scalar can be created. At sufficiently small length scale microscopic diffusion is significant and arrests the creation of smaller scale structures.

This process can be investigated by examining the wave number power spectrum of the passive scalar, which is the Fourier transform of the correlation function defined by

$$C(\vec{r}, t) = \langle \phi(\vec{x} + \vec{r}, t) \phi(\vec{x}, t) \rangle - \langle \phi(\vec{x}, t) \rangle^2, \quad (1)$$

<sup>a)</sup>Also at Department of Electrical Engineering.

where  $\phi(\vec{x}, t)$  is the passive scalar.

One can introduce the one dimensional power spectrum by averaging over all directions, i.e.,

$$F(k, t) = \int \frac{d^D \vec{k}'}{(2\pi)^D} \delta(k - |\vec{k}'|) \bar{C}(\vec{k}', t), \quad (2)$$

where  $D$  is the dimensionality of the integral domain and

$$\bar{C}(\vec{k}', t) = \int d^D \vec{r} C(\vec{r}, t) \exp(-i\vec{k}' \cdot \vec{r}) \quad (3)$$

is the  $D$ -dimensional power spectrum. The  $\phi$  variance is transported from small wave numbers to large wave numbers and dissipated at the upper end of the  $k$  spectrum. The cutoff of the power spectrum is determined by diffusivity. We are interested in the power spectrum that results when a temporally steady external source varying on some length scale  $L$  continually injects scalar into the fluid.

For turbulent flows with high Schmidt number ( $\nu/\kappa$ , where  $\nu$  is the kinematic viscosity, and  $\kappa$  is the diffusivity of the scalar), there is a range of wave numbers for which the flow energy has dissipated, while the diffusivity is still negligible. Put another way, there is a range of scalar lengths over which the flow is smooth but the scalar has rapid variations. This range is called the viscous-convective range. The power spectrum in the viscous-convective range has been predicted by Batchelor<sup>1</sup> to have the form  $F(k) \sim 1/k$ . This relation is widely known as the Batchelor's law. We note that Batchelor's reasoning is not confined to high Reynolds number turbulent flows. In particular, the requisite stretching is also present in low Reynolds number flows that are Lagrangian chaotic.

A number of experiments<sup>2</sup> and numerical simulations<sup>3</sup> have been carried out to check Batchelor's law. However, the results were inconclusive. For example, recent experiments of Williams *et al.*<sup>4</sup> have found a significant deviation

from Batchelor's law. These experiments were performed on a pseudo two dimensional turbulent flow. In their data, Batchelor's law holds, if at all, only at the very beginning of the viscous-convective range, where the flow can be envisioned as resulting from localized vortices.

In this paper we study Batchelor's law in two dimensional incompressible chaotic flows, using a wave-packet method introduced by Antonsen *et al.*<sup>5,6</sup> Based on this method we derive a simple form of the power spectrum [Eq. (16)] for flows in which intermittency of stretching is not negligible. To test our prediction we study three different model flows. The first model (Sec. III A) is a spatially periodic temporally irregular flow whose velocity field consists of a few sinusoids with wavelength  $L$ . The second model (Sec. III B) is a flow generated by a small number of self-consistently evolving point vortices in a circular cylinder. Aref<sup>7</sup> noticed that chaotic flows can be generated by a few vortices. His observation makes it possible for us to use a simple Lagrangian representation to study chaotic flows. Our vortex flow model is designed in the same spirit and is intended to be more similar than the first model to the flows in the Williams *et al.* experiment. The two models differ in the distribution of stretching for different areas of the fluid. The first model has a relatively uniform distribution of stretching, whereas the flow generated by self-consistently evolving vortices can have stretching that is intermittent, that is, different regions of the flow have greatly different stretching rates. Thus, for those fluid elements that repeatedly visit different regions, the rate of stretching varies greatly along their trajectories. For both models, we observe the  $k^{-1}$ -scaling range. For the third model (Sec. III C) we generate a velocity field adjusted to be similar to that in the experiment of Williams *et al.* by solving the initial value problem of the Navier–Stokes equation. We then obtain the power spectrum by taking the Fourier transform of the solution of the passive scalar partial differential equation (PDE) for  $\phi(\vec{x}, t)$ . These results are found to be in good agreement to results obtained for the same flow by use of the wave-packet method. Again we observe a clear  $k^{-1}$  scaling range.

In the paper of Williams *et al.*,<sup>4</sup> three possible reasons that might explain the observed absence of a clear  $k^{-1}$  scaling are mentioned: (1) intermittency of the flow; (2) residual three dimensional variations in the passive scalar flow in their supposed two dimensional configuration; (3) the localization of the scalar source and sink near the boundaries of the fluid. Our results strongly suggest that (1) is not a tenable reason. Nevertheless we do find a significant effect of intermittency. In particular, increased intermittency tends to make the roll-off at the end of the  $k^{-1}$  scaling range more gradual. This role of stretching intermittency has already been discussed by Kraichnan.<sup>8</sup>

## II. WAVE-PACKET METHOD

In previous work a wave-packet method was introduced for the study of passive scalar dynamics,<sup>5,6</sup> and numerical experiments with this method were shown to be in close agreement with full numerical solutions of the PDE governing the passive scalar [Eq. (4) below]. Since the wave-packet

method is much less computationally costly and since it gives insight into the physical mechanisms controlling the power spectrum, we use it as the basis of our study in this paper. (Section III C contains a comparison of the wave-packet method and direct solution of the passive scalar partial differential equation.)

We now review aspects of the wave-packet method that are important for our current work. The transport equation for a passive scalar field  $\phi(\vec{x}, t)$  is

$$\frac{\partial \phi}{\partial t} + \vec{v}(\vec{x}, t) \cdot \nabla \phi = \kappa \nabla^2 \phi + S_\phi(\vec{x}, t), \quad (4)$$

where  $\vec{v}(\vec{x}, t)$  is the velocity field, and  $S_\phi(\vec{x}, t)$  represents an external source. We assume the fluid flow is incompressible;  $\nabla \cdot \vec{v} \equiv 0$ . Neither the source nor the velocity field is affected by  $\phi$ .

At a length scale that is much smaller than the variations of  $S_\phi$ , the distribution of the scalar can be treated as consisting of a large number of sinusoidal wave packets, which are themselves convected by the fluid flow and are affected by diffusion. At a fixed time  $t$ ,  $\phi = \sum_j \phi_j$ , where  $\phi_j = A_j \sin(\vec{k}_j \cdot \vec{x} + \theta_j)$  represents the  $\phi$  distribution on the  $j$ th wave packet ( $A_j$  varies on a length scale  $\ell \ll L$  that is much larger than  $|\vec{k}_j|^{-1}$  and localizes  $\phi_j$  in space). In these terms, the power spectrum has the form of

$$F(k, t) = \sum_j F_j(k, t) = \sum_j w_j(t) \delta_\ell(k - |\vec{k}_j(t)|), \quad (5)$$

where  $w_j(t) = \int \phi_j^2 d^D x$ , and  $\delta_\ell(k - |\vec{k}_j|)$  represents a function of width  $\ell^{-1}$  in  $k$  centered at  $k = |\vec{k}_j|$  with  $\int \delta_\ell dk \equiv 1$ . The exact form of  $\delta_\ell$  and the value of  $\ell$  are unimportant provided  $L \gg \ell \gg k^{-1}$ . [Thus, in principles each  $F_j(k, t)$  is a smooth function which concentrates in a neighborhood of  $|\vec{k}_j|$ , and  $F(k, t)$  is also a smooth function. However, for the purpose of making a histogram approximation to  $F(k, t)$ , we may sample over a large number of wave packets and treat  $\delta_\ell$  as a delta function. The histogram made in this way asymptotes to the true histogram as the number of samples asymptotes to infinity.]

We are interested in applying Eq. (5) in two cases: (a) There is no scalar source ( $S_\phi \equiv 0$ ), but we assume that at  $t = 0$  there is a distribution of scalar density with initial wave-number spectrum concentrated at low  $k$  which we represent as  $F_I(k, t=0) = \sum_j w_j(0) \delta_\ell(k - |\vec{k}_j(t=0)|)$  (here the subscript  $I$  denotes "initial value problem"). (b) The scalar source continually injects passive scalar density at low  $k$  at a constant rate, and we represent this by continually introducing wave packets at low  $k$  into the sum in (5). In case (a), as  $t$  increases and the wave number  $k_j$  evolves into the diffusive range, the wave-packet variances decay and  $F_I(k, t \rightarrow \infty) \rightarrow 0$ . In case (b), the loss of wave packets through diffusion at high  $k$  is balanced by the injection of wave packets (by the source) at low  $k$ , and a time averaged steady state wave-number spectrum  $F_S(k)$  results (here the subscript  $S$  denotes "steady state").

In the absence of a source and diffusivity,  $w_j(t)$ , the variance of the  $j$ th wave packet, is constant in time. The evolution of  $\vec{k}_j$  can be determined as follows. Since the trajectory of a fluid element is given by

$$\frac{d\vec{\xi}}{dt} = \vec{v}(\vec{\xi}, t), \tag{6}$$

with initial condition  $\vec{\xi}(0) = \vec{x}$ , the separation of two elements that are initially close to each other,  $\delta\vec{\xi}(\vec{x}, t)$ , evolves as

$$\frac{d\delta\vec{\xi}(\vec{x}, t)}{dt} = (\delta\vec{\xi}(\vec{x}, t) \cdot \nabla) \vec{v}. \tag{7}$$

In the absence of a source and with zero diffusivity, Eq. (4) says that the scalar field is constant along each trajectory. Thus the difference of the scalar fields  $\delta\phi$  between the two trajectories separated by  $\delta\vec{\xi}$  is also constant in time. Since  $\delta\phi = \delta\vec{\xi} \cdot \nabla\phi$ , we have  $d(\nabla\phi \cdot \delta\vec{\xi})/dt = 0$ . Thinking of  $\phi$  as sinusoidal,  $\nabla\phi \sim \vec{k}_j\phi$ , we have  $d(\vec{k}_j \cdot \delta\vec{\xi})/dt = 0$ . Using Eq. (7) then yields the evolution of the wave number following a wave packet.

$$\frac{d\vec{k}_j}{dt} = -\nabla(\vec{v} \cdot \vec{k}_j). \tag{8}$$

When the diffusivity is small but nonzero, the variance decays as

$$\frac{dw_j}{dt} = -2\kappa w_j k_j^2 \tag{9}$$

with initial condition  $w_j(0)$ , where  $k_j = |\vec{k}_j|$ . In this case, Eq. (8) still holds but extra arguments are needed (see the Appendix in Ref. 5).

As previously discussed, in the case of a statistically steady external source  $S_\phi(\vec{x}, t)$ , we can think of the source as continually launching wave packets at low  $k$  which then evolve by (8) to higher  $k$ . In this case, each small area contains many overlapping wave packets each created by the source at a different time. Since, appropriate to a chaotic flow, we assume that correlations decay exponentially rapidly, the correlation between different wave packets can be neglected. Thus, rather than continually adding new low- $k$  wave number wave packets to (5), it will also sometimes be convenient to represent the power spectrum for the steady state  $F_S(k)$  as the time integral of the power spectrum for the initial value problem  $F_I(k, t)$ ,<sup>9</sup>

$$F_S(k) = \int_0^\infty F_I(k, t) dt \\ = \int_0^\infty \sum_j \exp(-2\kappa\tau_j(t)k_j^2(t)) \delta_\nu(k - k_j(t)) dt, \tag{10a}$$

where we have taken  $w_j(0) \equiv 1$  (i.e., each wave packet has the same initial variance), and

$$\tau_j(t) = \frac{\int_0^t k_j^2(s) ds}{k_j^2(t)}. \tag{10b}$$

In general, a stretching direction may temporarily become a contracting direction, hence  $k_j(t)$  is not necessarily increasing at all times and may pass through a given fixed wave number  $k$  at several times. From Eq. (10) we obtain a contribution from each  $k_j$  at each time  $t_{j_i}(k)$  such that  $k_j(t_{j_i}) = k$ ,

$$F_S(k) \approx \sum_j \sum_{j_i} \frac{\exp(-2\kappa\tau_{j_i}k_j^2)}{|dk_{j_i}/dt|} \Big|_{t=t_{j_i}(k)} \\ = \sum_j \sum_{j_i} \frac{\exp(-2\kappa\tau_{j_i}k^2)}{|k\eta_{j_i}|}, \tag{11}$$

where  $\eta_{j_i} \equiv (k^{-1}dk/dt)|_{t=t_{j_i}}$  gives the instantaneous rate of stretching.

If the flow has uniform stretching and the rate of stretching is independent of time, as assumed by Batchelor, then  $k_j(t) \sim \exp(\bar{\eta}t)$ , where  $\eta = \bar{\eta}$  is the uniform rate of stretching.<sup>10</sup> So Eq. (10b) gives  $\tau = (2\bar{\eta})^{-1}[1 - \exp(-2\bar{\eta}t)]$ , for large  $t \gg 1/\bar{\eta}$ ,

$$\tau \approx \frac{1}{2\bar{\eta}}, \tag{12}$$

and Eq. (11) yields

$$F_S(k) \sim \frac{\exp(-\kappa k^2/\bar{\eta})}{k}. \tag{13}$$

For small  $k$ , Eq. (13) gives the  $k^{-1}$  scaling.

If the flow has substantial intermittency of stretching, then  $\tau_{j_i}$  has a nontrivial distribution. One model of this phenomenon<sup>5</sup> is that the values  $\tau_{j_i}(k)$  and  $\eta_{j_i}(k)$  at a particular wave number  $k$  can be considered to be random variables which are selected on the basis of a distribution  $M(\tau, \eta)$  independent of  $k$ . That is, if one integrates Eqs. (6), (8), and (10b) for an ensemble of initial conditions and constructs a histogram for the values  $(\tau_{j_i}, \eta_{j_i})$  the fraction falling in the range  $(d\tau, d\eta)$  centered at  $(\tau, \eta)$  would be  $M(\tau, \eta)d\tau d\eta$ . It was argued in Ref. 5 that  $M(\tau, \eta)$  should be independent of  $t$  for  $\eta t \gg 1$  since according to Eq. (10b) the value of  $\tau_j$  depends mostly on the rate of exponential growth in the recent past. Similarly,  $M(\tau, \eta)$  should be independent of  $k$  for  $k \gg 1/L$ . With these assumptions the power spectrum  $F_S(k)$  given by (11) can be expressed as

$$F_S(k) \sim \frac{1}{k} \int_0^\infty d\tau \int_{-\infty}^\infty d\eta \frac{M(\tau, \eta)}{|\eta|} \exp(-2\kappa\tau k^2). \tag{14}$$

Integrating over  $h$  gives another distribution

$$M^*(\tau) = \int_{-\infty}^\infty dh \frac{M(\tau, \eta)}{|\eta|}, \tag{15}$$

which is the distribution of  $\tau$  weighted by the average of the reciprocal of the stretching rate. Equation (14) then becomes

$$F_S(k) \sim \frac{1}{k} \int_0^\infty d\tau M^*(\tau) \exp(-2\kappa\tau k^2). \tag{16}$$

[In the case of uniform stretching  $M(\tau, \eta) = \delta(\tau - (2\bar{h})^{-1})\delta(\eta - \bar{h})$  and  $M^*(\tau) = \delta(\bar{h}\tau - \frac{1}{2})$ .]

The contribution of a small interval  $[\tau, \tau + d\tau]$  is given by  $k^{-1} \exp(-2\kappa\tau k^2)M^*(\tau)d\tau$ . Using previous arguments, each contribution has the  $k^{-1}$  scaling for small  $k$ . Therefore, there should be a range of  $k$  where the power spectrum should obey Batchelor's law, although the exact location and form of the cutoff where  $k^{-1}$  behavior begins to fail is in general not given by (13). In particular, Batchelor's formula (13) predicts a sharp roll-off when the variance starts to decay. However, when the flow has considerable intermittency of stretching, some wave packets remain unaffected by diffusion while others that were created at the same time may have started to decay. Due to the contribution of these slowly decaying wave packets, the power spectrum should have a smoother roll-off than is predicted by (13). This will be numerically confirmed in the next sections. Also, in the next section we will compare numerical results with (13) and (16).

### III. NUMERICAL EXPERIMENTS

Equations (6), (8), and (10) allow us to evaluate the power spectrum of the passive scalar numerically. For a flow whose velocity field  $\vec{v}(\vec{x}, t)$  is known, we can first simultaneously integrate Eqs. (6), (8), and (10b) to determine  $\vec{k}_j(t)$  and  $\tau_j(t)$ , and then sum over all wave packets and integrate over time [using Eq. (10a)] to get  $F_S(k)$ . We can also make histograms of  $M^*(\tau)$  by using Eq. (15) and compute  $F_S(k)$  by using Eq. (16).

#### A. Random-driven flow

In this and the following subsection, we take  $\kappa = 1.25 \times 10^{-6}$ . Consider the velocity field (see Ref. 5 for more detailed properties of this flow) given by

$$\vec{v}(\vec{x}, t) = U[\vec{e}_x f_1(t) \cos(2\pi y/L + \theta_1(t)) + \vec{e}_y f_2(t) \cos(2\pi x/L + \theta_2(t))] \quad (17)$$

which is periodic in  $x$  and  $y$  with period  $L$ . The functions  $f_1$  and  $f_2$  are periodic in time with period  $T$  [i.e.,  $f_{1,2}(t \pm T) = f_{1,2}(t)$ ] and are given by

$$f_1(t) = \begin{cases} 1 & \text{for } 0 \leq t < T/2 \\ 0 & \text{for } T/2 \leq t < T \end{cases}$$

and

$$f_2(t) = \begin{cases} 0 & \text{for } 0 \leq t < T/2 \\ 1 & \text{for } T/2 \leq t < T \end{cases}$$

The flow is in the  $x$  direction during the first half of each period and in the  $y$  direction during the second half. To simulate a temporally chaotic velocity field we choose the angles,  $\theta_1(t)$  and  $\theta_2(t)$  at random (with uniform distribution) in  $[0, 2\pi]$  at the beginning of each period and keep them constant during the whole period.

Equations (6) and (8) can be solved with  $\vec{v}$  given by Eq. (17) for the evolution over one period,

$$x_{n+1} = x_n + \frac{1}{2} UT \cos\left(\frac{2\pi}{L} y_n + \theta_{1n}\right), \quad (18)$$

$$y_{n+1} = y_n + \frac{1}{2} UT \cos\left(\frac{2\pi}{L} x_{n+1} + \theta_{2n}\right), \quad (19)$$

and

$$k_{y,n+1} = k_{y,n} + \frac{\pi UT}{L} \sin\left(\frac{2\pi}{L} y_n + \theta_{1n}\right) k_{x,n}, \quad (20)$$

$$k_{x,n+1} = k_{x,n} + \frac{\pi UT}{L} \sin\left(\frac{2\pi}{L} x_{n+1} + \theta_{2n}\right) k_{y,n+1}, \quad (21)$$

where the position of a wave packet and its wave number are calculated at time  $t = T, 2T, 3T$ , and so on.

Since the angles are randomly chosen between periods, there are no KAM surfaces. To see this we note that a KAM surface for a two-dimensional map is an invariant closed curve for that map. Thus mapping every point on the curve forward by one iteration (period) maps those points back on the curve. In our case, the map changes randomly from iterate to iterate. Hence a curve invariant to the map at one time will typically not be invariant to the map at a subsequent time. Thus there are no KAM surfaces, and we expect that the fluid is totally mixed as time evolves.

Numerical experiments were performed using  $100 \times 100$  initial conditions on a uniform grid and  $UT/L = 0.5$ . The average rate of stretching after time  $t = 100T$  is given by the leading Lyapunov exponent of the flow, numerically determined to be  $\langle h \rangle \approx 0.30 \pm 0.01$ , where the average is taken over all initial conditions. Since  $\langle h \rangle > 0$ , the flow is chaotic. A finite time Lyapunov exponent  $h(\vec{x}_0, t)$  for an initial condition  $\vec{x}_0$  and a time  $t$  can be computed as follows. Start at time 0 with initial condition  $\vec{x}_0$  and an initial differential displacement  $\delta\vec{\xi}_0$  from  $\vec{x}_0$ . Evolve the differential displacement forward in time following the orbit from  $\vec{x}_0$  to obtain the differential displacement  $\delta\vec{\xi}(t)$  at time  $t$ . The finite time exponent is then  $h(\vec{x}_0, t) = t^{-1} \ln[|\delta\vec{\xi}(t)|/|\delta\vec{\xi}_0|]$ . For two dimensional incompressible flows,  $h$  can also be evaluated through

$$h(\vec{x}_0, t) = t^{-1} \ln\left(\frac{|\vec{k}(t)|}{|\vec{k}_0|}\right). \quad (22)$$

In our numerical experiments, we compute  $h$  by using Eq. (22). For randomly chosen  $\vec{x}_0$  the quantity  $h(\vec{x}_0, t)$  is random, and we can define a corresponding probability density function  $P(h, t)$  which we call the stretching distribution. The stretching distribution,  $P(h, t)$ , for a realization of Eqs. (18) and (19), is shown in Fig. 1(a) at different times. For large  $t$ ,  $P(h, t)$  can be approximated<sup>11</sup> by  $\ln P(h, t) = -tG(h) + o(t)$ , or more informally

$$P(h, t) \sim \exp[-tG(h)], \quad (23)$$

where  $G(\hat{h}) = G'(\hat{h}) = 0$  at the minimum  $\hat{h}$  of  $G$ . The utility of the scaling form (23) is that it gives  $P(h, t)$ , a function of two variables  $(h, t)$ , in terms of a function of only one variable,  $G(h)$ . For the case where there are no KAM surfaces, earlier numerical experiments<sup>12</sup> have yielded close agreement with this form. Figure 1(a) shows plots of  $P(h, t)$  obtained by use of histograms at different time  $t$ . As expected from (23),  $P(h, t)$  narrows with increasing time. Plotting

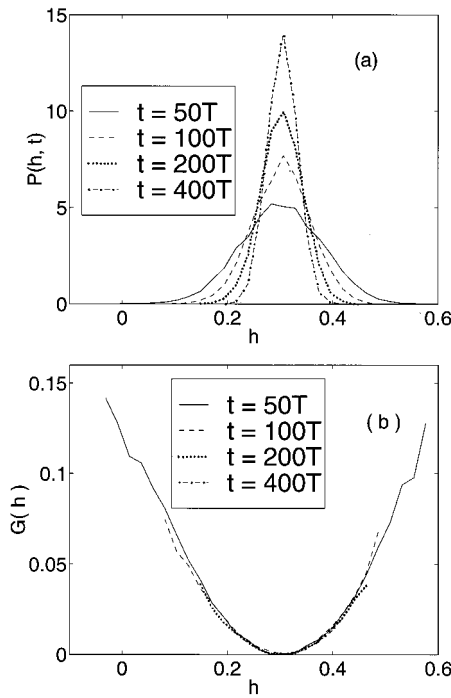


FIG. 1. (a) The distribution of the stretching factor at different times for the randomly driven flow  $\langle h \rangle \approx 0.30 \pm 0.01$ . (b) The large deviation approximation for the randomly driven flow, which is given by  $P(h, t) \sim \exp[-tG(h)]$ .

$-t^{-1} \ln P(h, t) - K$  [choosing  $K$  to be the minimum over  $h$  of  $-t^{-1} \ln P(h, t)$ ], we see from Fig. 1 that the data plotted in Fig. 1(b) collapses to a single curve, which we identify as  $G(h)$ . [This collapse is essentially the content of Eq. (23).] The distribution  $M^*(\tau)$  is discussed in the previous section and can be computed for a given  $k$  by first making a histogram of  $M(\tau, \eta)$  and then using (15). Figure 2 shows the distributions  $M^*(\tau)$  computed at several wave numbers. Note that the  $M^*(\tau)$  determinations obtained at different times are in good agreement with each other as expected.

In Fig. 3 we plot the power spectrum computed using Eqs. (6)–(10a) along with the power spectrum given by Eqs.

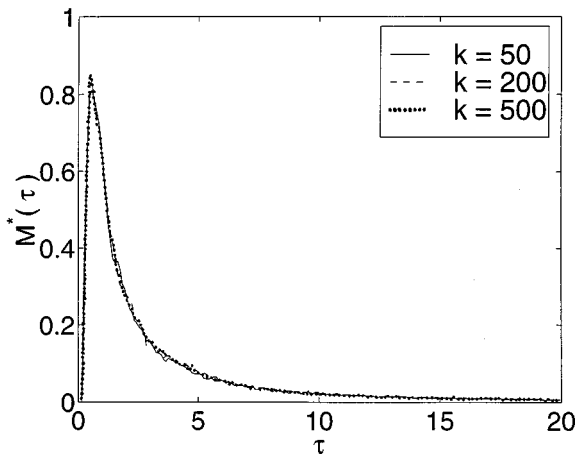


FIG. 2. The distributions of  $M^*(\tau)$  for the randomly driven flow, computed at different wave numbers.

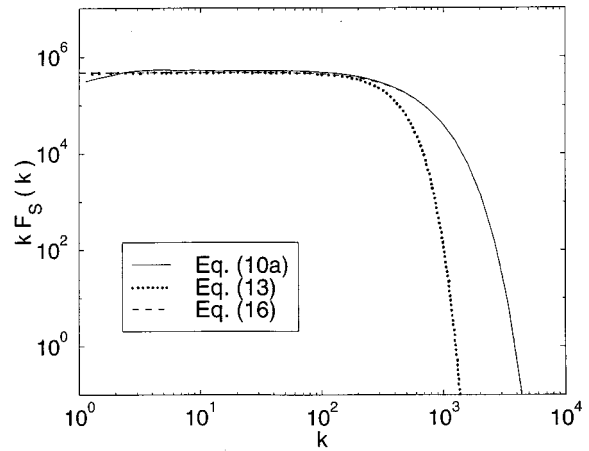


FIG. 3.  $kF_S(k)$  versus  $k$  for the random driven flow. The solid lines are computed from Eq. (10a), the dotted lines are computed from Eq. (13) (multiplied by an arbitrary constant), and the dashed lines are computed from Eq. (16).

(13) (based on uniform stretching) and (16) (which accounts for intermittency). For the wave-packet method, we replace (10a) by

$$F_S(k) = \sum_i \sum_j \exp[-2\kappa\tau_j(t_i)k_j^2(t_i)]\delta(k - k_j(t_i))\Delta t, \quad (24)$$

where  $\Delta t$  is the time step for the ODE solver and  $t_i = i\Delta t$ . Integrating (24) over a small interval  $[k, k + \Delta k]$  yields

$$F_S(k)\Delta k = \sum_{k \leq k_j(t_i) \leq k + \Delta k} \exp(-2\kappa\tau_j(t_i)k^2)\Delta t. \quad (25)$$

Equation (25) allows us to make histograms of  $kF_S(k)$  versus  $k$ . Equation (13) gives agreement with the wave-packet method [Eqs. (6)–(10a)] only before the cutoff of the spectrum. On the other hand, Eq. (16) agrees with the wave-packet method in the whole displayed region. We observe that the roll-off of the power spectrum is less sharp than the prediction of (13). This is because the flow has stretching intermittency, which is described by the distribution  $M^*(\tau)$ . The cutoff for different wave packets with different  $\tau$ 's, is spread over a wide range of  $k$ . In particular, the contribution from the wave-packets that decay only at a larger  $k$  are significant at the beginning of the roll-off. The number of such wave packets decreases continuously as  $k$  increases. This makes the roll-off less sharp.

**B. Vortex flow**

In this section we consider model flows for which the vorticity is concentrated on a finite number of point vortices located at  $\vec{x}_1, \vec{x}_2, \dots, \vec{x}_n$ . The use of such vortex flows to model physical velocity fields was introduced by Chorin<sup>13</sup> and has been used extensively. The velocity field induced by the  $j$ th vortex is given by

$$\vec{v}_j(\vec{x}) = \left[ -\frac{\Gamma_j}{2\pi} \left( \frac{y - y_j}{r_j^2} \right), \frac{\Gamma_j}{2\pi} \left( \frac{x - x_j}{r_j^2} \right) \right], \quad (26)$$

where  $r_j = \sqrt{(x - x_j)^2 + (y - y_j)^2}$ , and  $\Gamma_j$  is the strength of vortex  $j$  located at  $\vec{x}_j$ . Locally the flow rotates fluid elements

counterclockwise (clockwise) around the vortex if  $\Gamma_j > 0 (\Gamma_j < 0)$ . If the domain is the infinite plane, then the velocity field is the superposition of  $\vec{v}_j$ 's. That is,

$$\vec{v} = \sum_j \vec{v}_j. \tag{27}$$

If the domain has an impenetrable boundary,  $\partial D$ , then Eq. (27) needs to be modified to satisfy  $\vec{v} \cdot \vec{n} \equiv 0$  on  $\partial D$ . We consider the case where the domain  $D$  is a circular cylinder of radius one. In this case, the normal component of each  $\vec{v}_j$  on  $\partial D$  is cancelled by  $\vec{v}'_j$ , the velocity field induced by an image vortex of strength  $\Gamma'_j = -\Gamma_j$ , located at the mirror image of  $\vec{x}_j$ . The motion of each vortex is determined by all other vortices including image vortices. By Helmholtz's theorem for inviscid, incompressible flows, each  $\Gamma_j$  is constant in time. The equations of motion of the vortices are

$$\frac{dx_j}{dt} = -\frac{1}{2\pi} \sum_{i \neq j} \frac{\Gamma_i (y_j - y_i)}{r_{ji}^2} + \frac{1}{2\pi} \sum_{i,j} \frac{\Gamma_i (y_j - y'_i)}{r'_{ji}{}^2}, \tag{28}$$

$$\frac{dy_j}{dt} = \frac{1}{2\pi} \sum_{i \neq j} \frac{\Gamma_i (x_j - x_i)}{r_{ji}^2} - \frac{1}{2\pi} \sum_{i,j} \frac{\Gamma_i (x_j - x'_i)}{r'_{ji}{}^2}, \tag{29}$$

where

$$x'_i = x_i / (x_i^2 + y_i^2), \quad y'_i = y_i / (x_i^2 + y_i^2),$$

$$r_{ji} = \sqrt{(x_j - x_i)^2 + (y_j - y_i)^2},$$

$$r'_{ji} = \sqrt{(x_j - x'_i)^2 + (y_j - y'_i)^2}.$$

Equations (28) and (29) form a Hamiltonian system with Hamiltonian

$$H = \frac{1}{4\pi} \left\{ -\sum_{i \neq j} \Gamma_i \Gamma_j \log |\vec{x}_i - \vec{x}_j| + \sum_{i,j} \Gamma_i \Gamma_j \log |\vec{x}_i - \vec{x}'_j| + \sum_{i,j} \Gamma_i \Gamma_j \log |\vec{x}_i| \right\} \tag{30}$$

where  $(x_i, y_i)$  are the conjugate variables.

In addition to the Hamiltonian  $H$ , the angular momentum  $I = \sum_j \Gamma_j |\vec{x}_j|^2$  is also a constant of the motion. Therefore, a necessary condition for a system of such vortices to behave chaotically is that there are at least three vortices. Aref<sup>7</sup> showed numerically that three vortices can be sufficient for chaos. In this section we present numerical results from studying three model flows: (i) a flow generated by a system of three self-consistently evolving point vortices whose motion is integrable; (ii) a flow generated by a system of three point vortices whose motion is chaotic; and (iii) a flow generated by a system of six vortices whose motion is chaotic. Notice that the Lagrangian dynamics of a flow can be chaotic even if it is generated by vortices whose motion is integrable. (This situation is analogous to the restricted three body problem, where the motion of the two large bodies is described by Kepler orbits but the third infinitesimal body may move chaotically.)

For each case we consider initial conditions on a uniform grid of spacing 0.04. Equations (28) and (29) are solved, for each initial condition, by using a fourth order

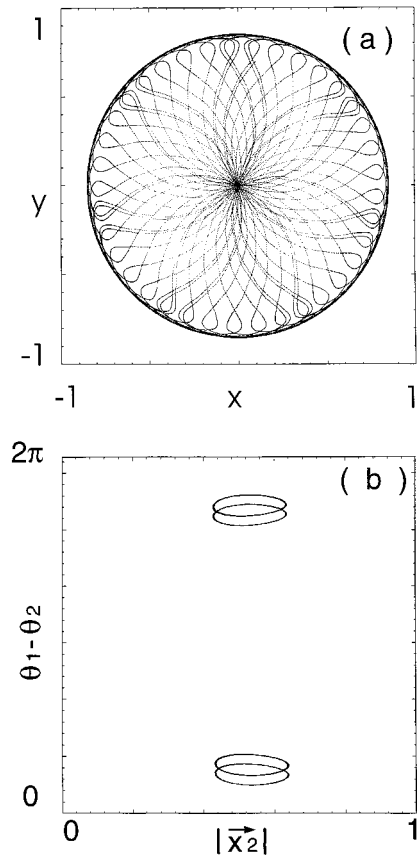


FIG. 4. (a) Regular trajectory  $\vec{x}_1(t)$  for an initial configuration given by  $\vec{x}_1(0)=(0.1,0.7)$ ,  $\vec{x}_2(0)=(0.5,0.5)$ ,  $\vec{x}_3(0)=(0.5,0.3)$ , and with  $-\Gamma_1=\Gamma_2=\Gamma_3=1$ . (b) The return map yields one dimensional closed curves, where  $\theta_1$  and  $\theta_2$  are the polar angles of  $\vec{x}_1$  and  $\vec{x}_2$ . The surface of section is taken at  $x_1^2+y_1^2=0.25$ .

Runge-Kutta method. Our statistics are based upon computation over these (approximately 2000) initial conditions.

In numerical experiments, we need to be concerned about the singularities at the location of the point vortices, where the velocity has infinite magnitude. These singularities may cause numerical problems. In addition, our assumption that the velocity field is relatively smooth is not valid near these singularities. To overcome these difficulties, we replace the point vortices by vortex patches, i.e., the vorticity is uniformly distributed in a small circle centered where the point vortices were, so that there are no singularities in the flow. We assume that the motion of the vortex patches can be described in the same way as the point vortices as long as they do not come too close to each other. This condition can be satisfied as we select the radii of the patches appropriately. We observe, however, that the results from using vortex patches and from using point vortices agree with each other.

### 1. Three integrable vortices

Figure 4(a) shows the trajectory of vortex 1,  $\vec{x}_1(t)$ , for the case where the initial configuration is given by  $\vec{x}_1(0)=(0.1,0.7)$ ,  $\vec{x}_2(0)=(0.5,0.5)$ ,  $\vec{x}_3(0)=(0.5,0.3)$ , and the vortex strengths are  $-\Gamma_1=\Gamma_2=\Gamma_3=1$ . The regular pattern of the trajectory is apparent, and suggests that the motion of

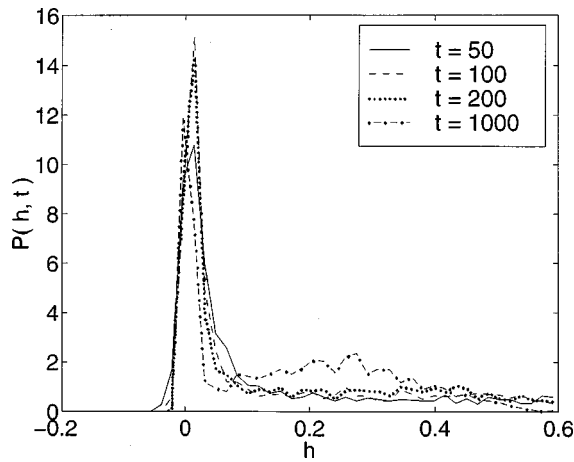


FIG. 5. The distribution of the stretching factor at different times for the flow induced by three integrable vortices,  $\langle h \rangle \approx 0.17 \pm 0.02$ .

the vortices is integrable (i.e., quasiperiodic). Figure 4(b) also confirms that the motion of the vortices is integrable. This figure shows the return map to the surface of section  $x_1^2 + y_1^2 = 0.25$ . The return map yields one dimensional closed curves, again implying quasiperiodic motion. Calculation of the trajectories of passive fluid elements for this flow suggest that the presence of both integrable and chaotic regions of space. The distribution of the finite time stretching rate  $h$  for  $10^4$  initial passive fluid element positions uniformly distributed in  $(x^2 + y^2) \leq 1$  is shown in Fig. 5. The distribution has a major peak near  $h=0$  and possibly a minor peak near  $h=0.25$ . The peak at  $h=0$  is due to the existence of initial conditions for which the passive scalar dynamics is integrable. The existence of a minor peak shows that for other trajectories the Lagrangian dynamics is chaotic. Such distributions have been previously discussed in Ref. 14.

Figure 6 shows the evolution of  $k_j$  for an arbitrarily chosen wave packet in the chaotic part of the phase space. It is observed that  $k_j$  sometimes increases in sudden bursts followed by long flat or more gently increasing ranges. We call such behavior intermittency. If we trace the trajectory of this wave-packet, we find that the bursts occur when it gets very

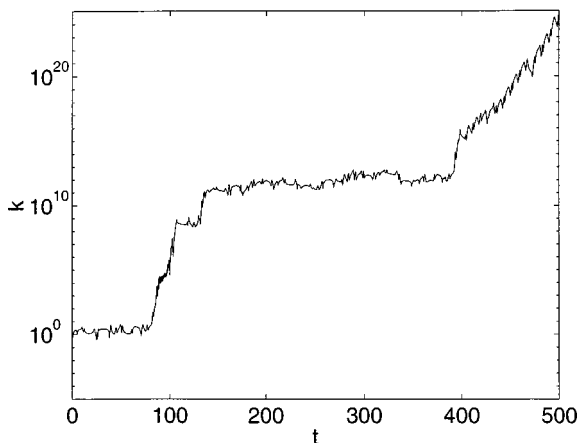


FIG. 6. The evolution of an arbitrarily chosen wave packet in the flow induced by three integrable vortices.

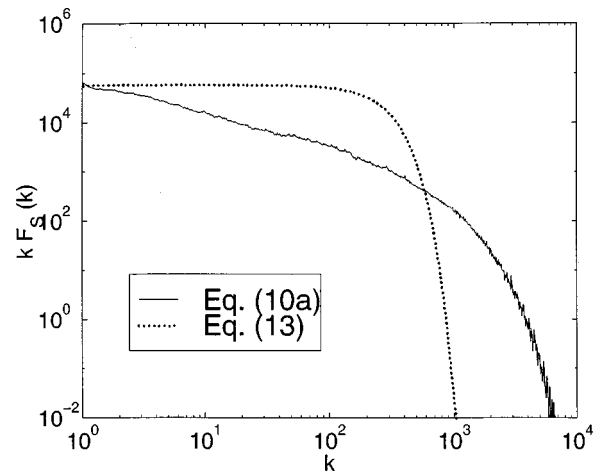


FIG. 7.  $k F_S(k)$  versus  $k$  for the flow generated by three integrable vortices. The solid lines are computed from Eq. (10a) and the dotted lines are computed from Eq. (13).

close to the two positive vortices, which move as they circle around each other.

Figure 7 shows the wavenumber power spectrum of the passive scalar computed from Eq. (10a). The spectrum for this case does not conform to Batchelor's  $k^{-1}$  law in any range of  $k$ . This is not surprising since Batchelor's argument assumes exponential stretching, and this does not apply for wave-packets in the quasiperiodic part of phase space.

### 2. Three chaotic vortices

Figure 8 shows the trajectory  $\vec{x}_1(t)$ , for the case where the initial configuration is given by  $\vec{x}_1(0) = (0.1, 0.7)$ ,  $\vec{x}_2(0) = (0.2, 0.9)$ ,  $\vec{x}_3(0) = (0.5, 0.3)$ , and the vortex strengths are  $-\Gamma_1 = \Gamma_2 = \Gamma_3 = 1$ . The trajectory is irregular, suggesting that the vortex motion is chaotic. This is confirmed by calculation of the leading Lyapunov exponent for the system of vortices (28) and (29), which is approximately 0.3. For the

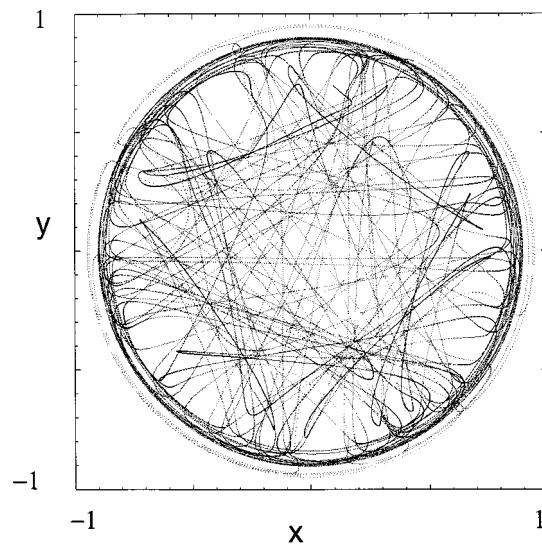


FIG. 8. The trajectory  $\vec{x}_1(t)$  is irregular, where the initial configuration is given by  $\vec{x}_1(0) = (0.1, 0.7)$ ,  $\vec{x}_2(0) = (0.2, 0.9)$ ,  $\vec{x}_3(0) = (0.5, 0.3)$ , and  $-\Gamma_1 = \Gamma_2 = \Gamma_3 = 1$ .

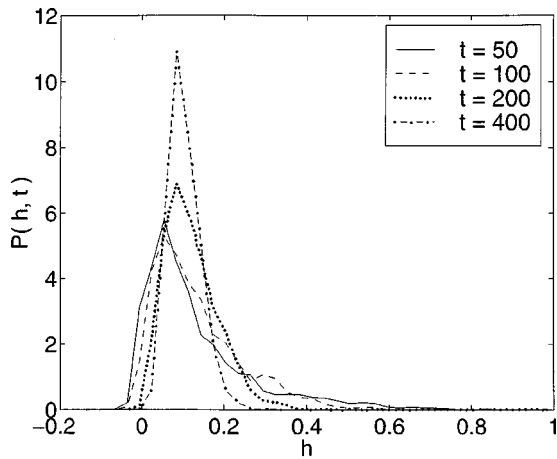


FIG. 9. The distribution of the stretching factor at different times for the flow induced by three chaotic vortices,  $\langle h \rangle \approx 0.12 \pm 0.02$ .

flow generated by these vortices, the spatially averaged Lyapunov exponent of passive advected particles is  $\langle h \rangle \approx 0.12 \pm 0.02$ . From Fig. 9 we see that there is one main peak in the distribution of  $h$  which is near  $\langle h \rangle$ , so the distribution is more uniform than that in the integrable case. However, compared to the randomly driven flow discussed earlier (Sec. III A), the peak is broader.

Figure 10 shows the evolution of  $k_j$  for an arbitrarily chosen wave packet. The growth of  $k_j$  is apparently less intermittent than the case for the three integrable vortices, Fig. 6. This difference appeared to hold for other random wave packet choices for the two flows.

Figure 11 shows the predictions of the spectrum  $F_S(k)$  from Eq. (13) (uniform stretching) as the dotted curve, Eq. (16) [the  $M^*(\tau)$  result] as the dashed line, and Eq. (10a) (the integral of  $F_S$ ) as the solid line. The predictions of Eq. (16) and Eq. (10a) are similar and significantly different from the prediction of Eq. (13). We believe that the small difference between the predictions of Eq. (16) and Eq. (10a) is due to insufficient mixing and the limitation of finite diffusion. In this case, the distribution  $M^*(\tau)$  depends on the wavenum-

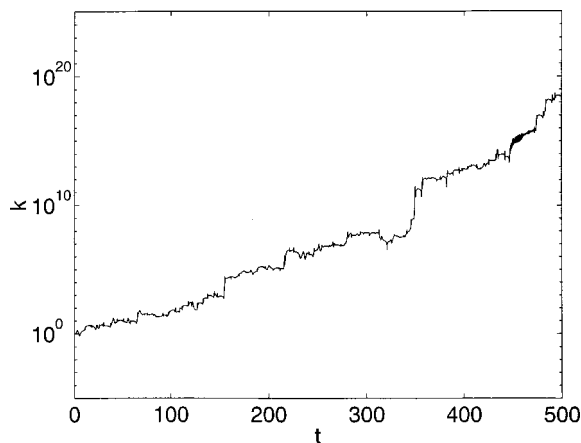


FIG. 10. The evolution of an arbitrarily chosen wave packet in the flow induced by three chaotic vortices.

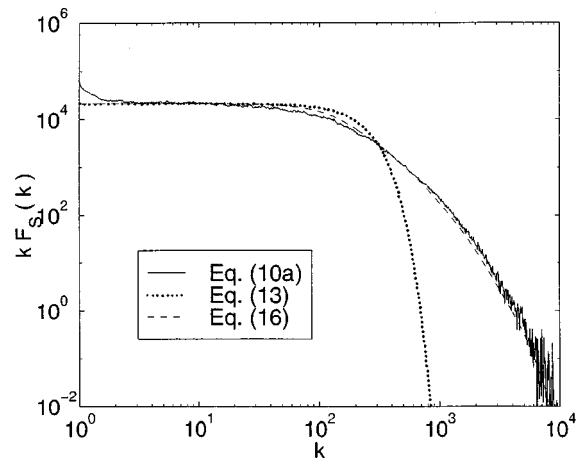


FIG. 11.  $k F_S(k)$  versus  $k$  for the flow generated by three chaotic vortices. The solid lines are computed from Eq. (10a), the dotted lines are computed from Eq. (13) (multiplied by an arbitrary constant), and the dashed lines are computed from Eq. (16).

ber  $k$ . This may also explain why the middle part of the power spectrum differs slightly from the  $k^{-1}$ -scaling.

### 3. Six chaotic vortices

In this section we focus on how the power spectrum is affected when the flow has more vortices. We study a flow generated by a system of six vortices whose initial configuration is given by  $\vec{x}_1(0) = (0.1, -0.2)$ ,  $\vec{x}_2(0) = (0.2, -0.8)$ ,  $\vec{x}_3(0) = (0.5, -0.5)$ ,  $\vec{x}_4(0) = (0.1, 0.5)$ ,  $\vec{x}_5(0) = (0.7, 0.1)$ ,  $\vec{x}_6(0) = (0.9, 0.2)$ , and whose strengths are  $-\Gamma_1 = \Gamma_2 = \Gamma_3 = -\Gamma_4 = -\Gamma_5 = -\Gamma_6 = 1$ . The leading Lyapunov exponent for the system of vortices is approximately 0.7, which is larger than in the previous cases. This is apparently because the stirring is stronger when there are more vortices in the flow. The spatially averaged rate of stretching is  $\langle h \rangle \approx 0.28 \pm 0.02$  (the distribution of  $h$  is presented in Fig. 12), so the flow is chaotic. The distribution of  $h$  is more uniform than the other vortex flows. Figure 13 shows that Eq. (16) (the dashed curve) agrees well with the power spectrum com-

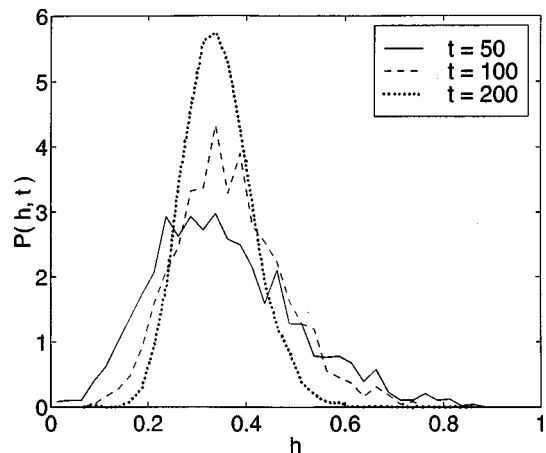


FIG. 12. The distribution of the stretching factor at different times for the flow induced by the flow induced by six chaotic vortices,  $\langle h \rangle \approx 0.35 \pm 0.02$ .

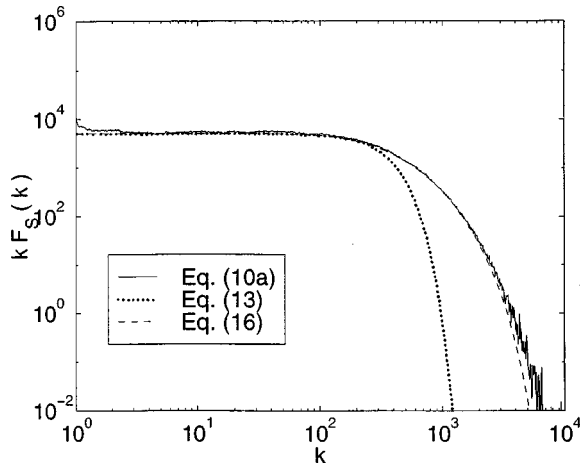


FIG. 13.  $kF_S(k)$  versus  $k$  for the flow generated by six chaotic vortices. The solid lines are computed from Eq. (10a), the dotted lines are computed from Eq. (13) (multiplied by an arbitrary constant), and the dashed lines are computed from Eq. (16).

puted from Eq. (10a) (the solid curve), but not with the result assuming uniform stretching (13) (the dotted line).

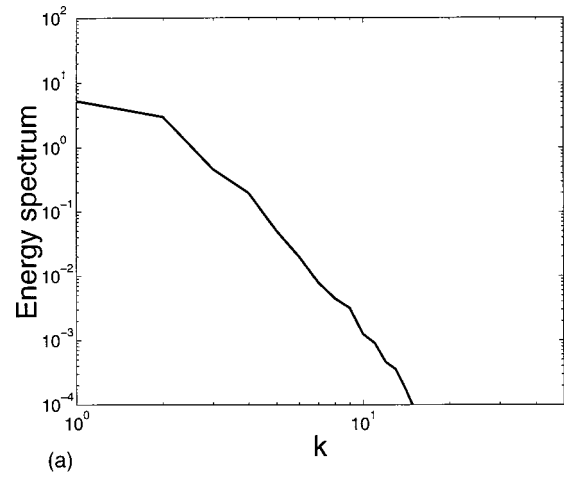
**C. Realistic flow**

The transport of a passive scalar field which is advected by a velocity field closely simulating the real velocity field of the experiment of Williams *et al.*<sup>4</sup> is investigated in this section. The velocity field is obtained by solving the two dimensional Navier–Stokes equation with a linear friction term

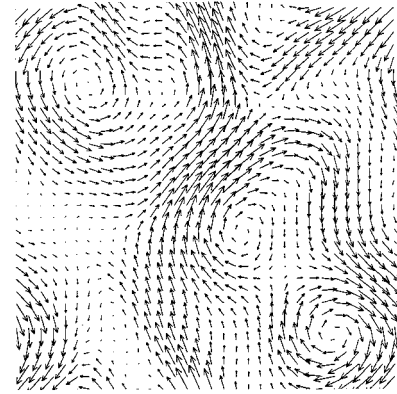
$$\frac{\partial \omega(\vec{x})}{\partial t} + \vec{v} \cdot \nabla \omega = \nu \nabla^2 \omega - \mu \omega + S_\omega(\vec{x}), \tag{31}$$

where  $\omega(\vec{x})$  is the scalar vorticity field ( $= \hat{z} \cdot \nabla \times \vec{v}$ ),  $\vec{v}$  is the velocity vector field,  $\nu$  is the kinematic viscosity,  $\mu$  is the linear friction coefficient,  $S_\omega(\vec{x})$  is a source of vorticity given by the curl of the stirring force field [ $= \hat{z} \cdot \nabla \times \vec{f}(\vec{x})$ ], where  $\vec{f}(\vec{x})$  is the stirring force field which in Ref. 4 is produced by a Lorentz force on the fluid due to the combined effect of permanent magnets placed under the fluid and an electrical current flowing through the fluid]. The above equation is obtained by taking the curl of the two dimensional Navier-Stokes equation with a linear friction term. The vorticity field is related to the stream function  $\psi(x,y)$  by  $\nabla^2 \psi = \omega$ , and the velocity field is related to the stream function by  $\vec{v} = -(\nabla \times \psi \hat{z})$ . The linear friction term models friction with the bottom of the container supporting the fluid layer.

Equation (31) for  $\omega$  and Eq. (4) for the passive scalar advection are solved numerically using a time split-step technique with periodic boundary conditions in  $x,y$ . A system size of  $[-\pi, \pi] \times [-\pi, \pi]$  is used. In the first phase of the split step the Laplacian parts of both equations are solved in wave number space with the source terms and the linear friction term included. For the vorticity field,  $\partial \omega / \partial t = \nu \nabla^2 \omega - \mu \omega + S_\omega(x,y)$  is solved by fast Fourier transforming to wave number space [ $\omega(x,y,t) \rightarrow \bar{\omega}(k_x, k_y, t)$ ], followed by  $\bar{\omega}(k_x, k_y, t + \Delta t) = \bar{\omega}(k_x, k_y, t) \exp[-(\nu k^2 + \mu) \Delta t] + \bar{S}_\omega(k_x, k_y) \Delta t$ , where  $\bar{S}_\omega(k_x, k_y)$  is the Fourier transform of



(a)



(b)

FIG. 14. (a) Power spectrum of velocity field (b) typical velocity field ( $t = 40$ ). The length of the arrows is proportional to the magnitude of velocity field at the corresponding grid point.

the vorticity source function.  $S_\omega(x,y) = \alpha \cos 2x(\cos 4y + 1)$  is used to give an approximated functional form for the stirring field used in the experiment of Williams *et al.* Then,  $\bar{\omega}(k_x, k_y, t + \Delta t)$  is transformed back to real space. The diffusive and source terms of the passive scalar field,  $\partial \phi / \partial t = \kappa \nabla^2 \phi + S_\phi(x,y)$ , are treated in a similar way, while, for the source function of the passive scalar,  $S_\phi(x,y) = \cos 2x + \cos 2y$  is used. In the second phase of the split step the convection parts of the vorticity field and the passive scalar field,  $\partial \omega / \partial t = -\vec{v} \cdot \nabla \omega$ ,  $\partial \phi / \partial t = -\vec{v} \cdot \nabla \phi$ , respectively, are solved in real space using the velocity field which is obtained from the stream function  $\psi(x,y)$  utilizing  $\vec{v} = -(\nabla \times \psi \hat{z})$ . [We note that our choice of  $S_\phi(x,y)$  is different from the experiment, where dye is introduced at the boundary of the flow; see Ref. 4.]

Figure 14(a) shows the energy spectrum for the velocity field of the numerical solution with the grid size of  $1024^2$ ,  $\nu = 0.005$ ,  $\mu = 0.12$ . The value of  $\mu$  was chosen to match the value for the experiment in Ref. 4, while  $\nu$  was adjusted so that the resulting flows resembled the measured flows of Ref. 4. The energy spectrum of the velocity field is obtained in the following way. The energy density at a given wavevector  $\vec{k}$  is evaluated by

$$E(\vec{k}) = \frac{1}{2} (|\bar{v}_x(\vec{k})|^2 + |\bar{v}_y(\vec{k})|^2) \tag{32}$$

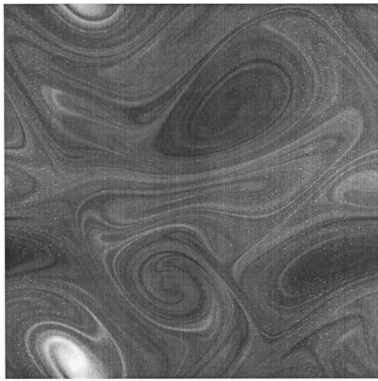


FIG. 15. Passive scalar field at  $t=45$ .

where  $\tilde{v}_x(\vec{k}), \tilde{v}_y(\vec{k})$  are Fourier transformations of  $v_x(\vec{x}), v_y(\vec{x})$ , respectively. Then the energy spectrum  $E(k)$  is calculated by

$$E(k) = \int E(\vec{k}') \delta(|\vec{k}'| - k) d^2\vec{k}'. \quad (33)$$

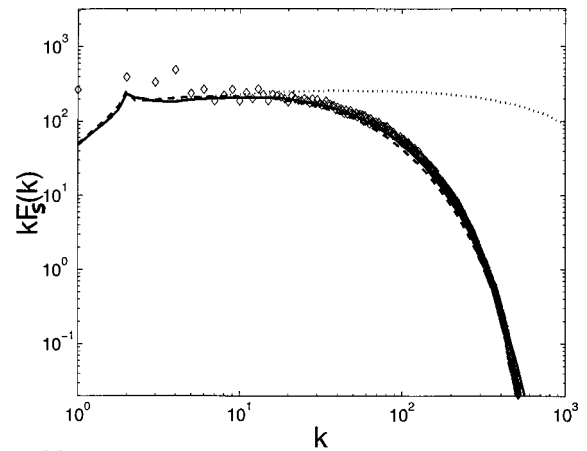
The energy of the field at  $\log_{10} k \sim 1$  or  $k \sim 10$  is almost  $10^4$  times smaller than that at the lowest  $k$  in Fig. 14(a). So the velocity field with smaller scale than  $L \sim 2\pi/10$  does not fluctuate much, which will justify our linear interpolation approximation of the velocity field at the smaller scale later. A typical velocity field is shown in Fig. 14(b). During the course of the simulation, there are typically 3~5 large vortex structures visible in the system.

After the initial transient time, the passive scalar field, which is continuously influxed at the large scale, is evolved to a field which has very small length scale due to stretching and folding by the velocity field. Figure 15 shows a well developed passive scalar field with a diffusivity  $\kappa = 2.5 \times 10^{-5}$ . The power spectrum of the passive scalar is measured during the simulation at every 2.5 time units. The time averaged spectrum is obtained by averaging these instantaneous spectra.

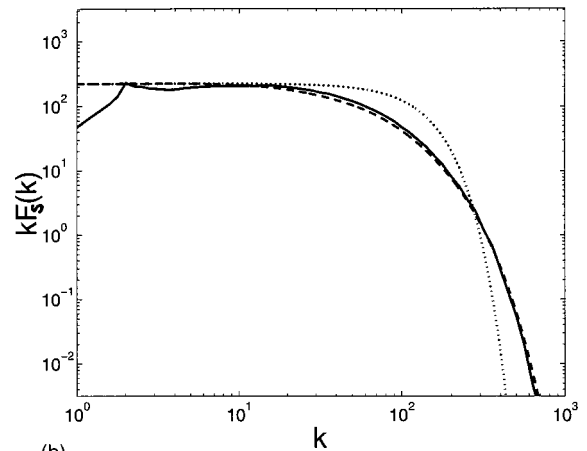
$$\langle F(k) \rangle = \sum_{i=1}^N F_I(k, t_i) \zeta_i, \quad (34)$$

where the weighting factor  $\zeta_i = 1/\int dk F(k, t_i)$ ,  $t_i = T_0 + (i - 1)\Delta T$ ,  $\Delta T = 2.5$ , and  $i = 1, \dots, 17$ .  $T_0$  is selected to be large enough to give full development of the passive scalar spectrum in the viscous-convection range. Here we choose  $T_0 = 30$  (assuming  $k \sim k_0 e^{\langle h \rangle t}$  with the measured  $\langle h \rangle \sim 0.208$ ,  $k$  becomes  $\sim 1.0 \times 10^4$  by the time  $t = T_0 = 30$ , which is much bigger than the cutoff wave number). The diamonds in Fig. 16(a) show the time averaged spectrum  $\langle F(k) \rangle$ .

The power spectrum of the passive scalar is also obtained using the wave-packet method. The derived velocity field from solution of (31) is used for the advection of the passive scalar wave packets. Since, with the given viscosity, the velocity field can be calculated in fairly coarse resolution ( $32 \times 32$  or  $64 \times 64$ ), to increase the computational efficiency without losing the details of velocity field, a linear interpolation between grid points is utilized to obtain  $\vec{v}(\vec{x})$  and  $\nabla \vec{v}(\vec{x})$  for any location of a passive scalar wave packet. The



(a)



(b)

FIG. 16. (a)  $kF_S(k)$  of passive scalar. Diamonds are from the full numerical simulations with the time average over  $t = [30, 70]$ ; the solid line and the dashed line are results from the wave-packet method with the initial and the continuous input of passive scalar wave packets, respectively. The dotted line is for a smaller diffusion coefficient,  $\kappa = 1.0 \times 10^{-6}$ . (b) The solid line is the result from the wave-packet method with the initial input of passive scalar wave packets. The dashed line is from Eq. (16). The dotted line is the result from Eq. (13) (multiplied by an arbitrary constant).

passive scalar wave packets are injected initially (or continuously) uniformly over the space investigated. Initial wave vectors for passive scalar wave packets are set to  $(2, 0)$  which corresponds to the major wave vector of the source function for the full numerical computations in Eq. (4).

The obtained power spectra of the passive scalar are shown in Fig. 16(a). The solid line is the time integrated passive scalar power spectrum obtained from Eq. (10a), where  $F_1$  is obtained by initially starting with a large number of passive scalar wave packets. The dashed line is the power spectrum computed from Eqs. (5)–(9) for the case when the passive scalar wave packets are continuously injected to the system at low  $k$ . For the second case, the power spectrum is obtained by a time average of the instantaneous power spectrum over  $T = [30, 300]$ . The diamonds are from full numerical integration of (4). For all these cases, the same diffusivity  $\kappa = 2.5 \times 10^{-5}$  is used. We find very good agreement between the full numerical simulation of passive scalar advection [diamonds in Fig. 16(a)] and the two results from the wave-packet method. The deviation at low wavenumbers is

due to the fact that the passive scalar injected at low wave numbers is not well approximated in the wave-packet approximation. The dotted line in Fig. 16(a) is the case when a smaller diffusivity coefficient ( $\kappa=1\times 10^{-6}$ ) is used for a wave-packet method simulation with the same flow. When the diffusion coefficient is low, Batchelor's  $k^{-1}$  law is very clearly observed over a large range in  $k$  before the roll-off due to diffusivity. In Fig. 16(b), the power spectrum from Eq. (16) (dashed line) is compared to the result of the wave-packet simulation (10a) (solid line). The agreement among these results is good, but there is significant deviation from Batchelor's formula (13) (dotted line).

#### IV. CONCLUSION

We have studied the power spectra of passive scalars in several model flows. For most of the chaotic flows that we studied, we observe a  $k^{-1}$ -scaling region in the power spectrum, as predicted by Batchelor. For the case in Sec. III B 1 the power spectrum deviates from the  $k^{-1}$ -scaling, and we argue that this is due to insufficient mixing combined with finite diffusion. On the other hand, when the flow has strong intermittency, for example, when there are highly-localized, long-lasting vortices (as in Secs. III B 2 and III B 3), the roll-off of the power spectrum tends to be smoother than predicted by (13). In this case, Eq. (16) gives a better prediction.

In their experiments Williams *et al.*<sup>4</sup> observed significant deviation from Batchelor's  $k^{-1}$  scaling, for which our analysis cannot account. There may be additional mechanisms causing this deviation in their experiments which has not yet been understood. One explanation may come from the fact that the flows in their experiments were not exactly two dimensional, and this possible effect was discussed in detail in Ref. 4. An additional possible explanation may be related to the method of injecting a scalar (a fluorescent dye) from one end and extracting it from the other end of the container. The effect of this on the wavenumber spectrum will be reported elsewhere.<sup>15</sup>

#### ACKNOWLEDGMENTS

This work was supported by ONR (Physics) and DOE. We thank J. P. Gollub for useful discussions.

- <sup>1</sup>G. K. Batchelor, "Small-scale variation of convected quantities like temperature in turbulent fluid," *J. Fluid Mech.* **5**, 113 (1959).
- <sup>2</sup>C. H. Gibson and W. H. Schwarz, "The universal equilibrium spectra of turbulent velocity and scalar fields," *J. Fluid Mech.* **16**, 365 (1963); H. L. Grant, B. A. Hughes, W. M. Vogel, and A. Moilliet, "The spectrum of temperature fluctuations in turbulent flow," *ibid.* **34**, 423 (1968); P. L. Miller and P. E. Dimotakis, "Measurements of scalar power spectra in high Schmidt number turbulent jets," *ibid.* **308**, 129 (1996); J. O. Nye and R. S. Brodkey, "The scalar spectrum in the viscous-convective sub-range," *ibid.* **29**, 151 (1967); X.-L. Wu, B. Martin, H. Kellay, and W. L. Goldburg, "Hydrodynamic convection in a two-dimensional Couette cell," *Phys. Rev. Lett.* **75**, 236 (1995).
- <sup>3</sup>M. Holzer and E. D. Siggia, "Turbulent mixing of a passive scalar," *Phys. Fluids* **6**, 1820 (1994); D. Bogucki, J. A. Domaradzki, and P. K. Yeung, "Direct numerical simulations of passive scalars with  $P\tau > 1$  advected by turbulent flow," *J. Fluid Mech.* **343**, 111 (1997); R. T. Pierrehumbert, "Tracer microstructure in the large-eddy dominated regime," *Chaos, Solitons and Fractals* **4**, 1091 (1993).
- <sup>4</sup>B. S. Williams, D. Marteau, and J. P. Gollub, "Mixing of a passive scalar in magnetically forced two-dimensional turbulence," *Phys. Fluids* **9**, 2061 (1997).
- <sup>5</sup>T. M. Antonsen, Jr., Z. Fan, E. Ott, and E. Garcia-Lopez, "The role of chaotic orbits in the determination of power spectrum of passive scalars," *Phys. Fluids* **8**, 3094 (1996).
- <sup>6</sup>T. M. Antonsen, Jr., Z. Fan, and E. Ott, " $k$  spectrum of passive scalars in Lagrangian chaotic fluid flows," *Phys. Rev. Lett.* **75**, 1751 (1995).
- <sup>7</sup>H. Aref, "Integrable, chaotic, and turbulent vortex motion in two-dimensional flows," *Annu. Rev. Fluid Mech.* **15**, 345 (1983).
- <sup>8</sup>R. H. Kraichnan, "Small-scale structure of a scalar field convected by turbulence," *Phys. Fluids* **11**, 945 (1968).
- <sup>9</sup>T. M. Antonsen, Jr. and E. Ott, "Multifractal power spectra of passive scalars convected by chaotic fluid flows," *Phys. Rev. A* **44**, 851 (1991).
- <sup>10</sup>In fact,  $k_j(t) \sim \exp(|h_2|t)$ , where  $h_2$  is the negative Lyapunov exponent. Since the flow is incompressible, the positive Lyapunov exponent (or the rate of stretching) is  $h_1 = |h_2|$ . However, if the flow is three dimensional, then in general the growth rate of  $k_j$  is different from the rate of stretching.
- <sup>11</sup>P. Grassberger, R. Badii, and A. Politi, "Scaling laws for invariant measures on hyperbolic and nonhyperbolic attractors," *J. Stat. Phys.* **51**, 135 (1988).
- <sup>12</sup>F. Varosi, T. M. Antonsen, Jr., and E. Ott, "The spectrum of fractal dimensions of passively convected scalar gradients in chaotic fluid flows," *Phys. Fluids A* **3**, 1017 (1991).
- <sup>13</sup>A. J. Chorin, "Numerical study of slightly viscous flow," *J. Fluid Mech.* **57**, 785 (1973).
- <sup>14</sup>M. A. Sepúlveda, R. Badii, and E. Pollak, "Spectral analysis of conservative dynamical systems," *Phys. Rev. Lett.* **63**, 1226 (1989); T. Horita, H. Hata, R. Ishizaki, and H. Mori, "Long-time correlations and expansion rate spectra of chaos in Hamiltonian systems," *Prog. Theor. Phys.* **83**, 1065 (1990).
- <sup>15</sup>K. Nam, T. M. Antonsen, P. N. Guzdar, and E. Ott, " $k$  spectrum of finite lifetime passive scalars in Lagrangian chaotic fluid flows," *Phys. Rev. Lett.* **83**, 3426 (1999).